2-1-2016

Particle-in-Cell Simulations Examining AK Gap Closure Mechanisms in the Pinch Reflex Diode

Elizabeth Madrid

_____
Candidate

_____
Department

This thesis is approved, and it is acceptable in quality and form for publication:

Approved by the Thesis Committee:

_____, Chairperson

_____

_____

_____

_____

_____

_____

_____

Particle-in-Cell Simulations Examining AK Gap Closure Mechanisms in the Pinch Reflex Diode

by

Elizabeth A. Madrid

B.S., New Mexico Institute of Mining and Technology, 2007

THESIS

Submitted in Partial Fulfillment of the
Requirements for the Degree of

Master of Science
Electrical Engineering

The University of New Mexico

Albuquerque, New Mexico

December 2015

Dedication

Above all others, to God through whom this was possible; to my loving husband, Alfonso, for his support, encouragement, and inspiration; and to my sister, Meredith, who supported the decision to get my degree at the cost of our time together.

Acknowledgments

Particle-in-Cell Simulations Examining AK Gap Closure Mechanisms in the Pinch Reflex Diode

by

Elizabeth A. Madrid

B.S., New Mexico Institute of Mining and Technology, 2007

M.S., Electrical Engineering, University of New Mexico, 2015

Abstract

Gap closure mechanisms in the pinch reflex diode are studied using cylindrical, two-dimensional, fully kinetic, electromagnetic, particle-in-cell simulations. The key physical dimensions in the model are based on the Mercury accelerator at the Naval Research Laboratory in Washington, DC. Simulation results agree well with theoretically predicted currents and impedances as well as with experimental values. The effects of cathode plasma formation with various desorption rates are studied. Also examined are different cathode plasma species including H, H_2, N_2, H_2O, and C. While the presence of heavier plasma species results in lower ion current production, total diode current and voltage are not impacted. Charge exchange between neutral H_2 and H_2^+ yields a decrease in ion current but does not result in a decreased anode-cathode gap. In the short-pulse limit studied here, charge exchange is not found to be a dominating factor in pinch reflex diode impedance collapse.

Contents

Contents

List of Figures

Chapter 1

Introduction

1.1 Ion Diodes

Ion diodes have been primarily used on pulsed power accelerators for inertial confinement fusion research and are finding new applications in materials processing and as magnetic fusion diagnostics [1]. More recently, ion diodes are being used to produce gamma radiation and induce photofission in a given sample [2]. The ion diodes discussed herein create intense ion flows and employ space-charge-neutralized beam transport and electrostatic acceleration. These diodes convert high electrical-power pulses into ion beams. These beams range in energy from 50 keV to 10 MeV with ion currents ranging from 1 kA to 10 MA and durations up to 1 μs [1]. Diode impedances range from 1 Ω to 20 Ω [3]. Depending on the application, different beam properties are of interest, including but not limited to energy density, current density, divergence, uniformity, reproducibility, and atomic composition. Ion generation efficiency, the ratio of ion to total diode current, can reach up to 60% for lower impedance diodes and as low as 20% for higher impedance diodes [3]. The Child-Langmuir formula gives the nonrelativistic approximation for maximum space-charge-limited current densities for electrons and ions flowing in an ion diode

$$j_{e,i} = \left(\frac{2e}{m}\right)^{1/2} \frac{V_0^{3/2}}{9\pi d^2},$$

(1.1)

1

where e is the electron or ion charge, m is the electron or ion mass, V_0 is the applied voltage, and d is the anode-cathode (AK) gap of the diode.

Two types of ion diodes that aim to control the low efficiency of bipolar flow via high field-stress operation are the applied magnetic field ion diode that aims to control electron motion, and the pinch-reflex diode (PRD) that increases electron path length. Ion diodes exhibit early AK gap closure and related impedance collapse that results in overall reduced ion power on target [4].

1.2   Applied Magnetic Field Ion Diode

The applied magnetic field diode utilizes a transverse magnetic field, known as the critical field, in the AK gap. This field causes the less massive electrons to turn back on their original trajectory while allowing the more massive ions to continue on their original trajectory with minimal interference. A simple diagram of the magnetically insulated diode can be found in Fig. 1.1.

The critical field is determined in a gap with a voltage V_0, by

$$\int B * dx = \left(\frac{2eV_0}{r_e}\right)^{1/2} \left(\frac{1 + eV_0}{2m_e c^2}\right)^{1/2}, \tag{1.2}$$

where e is the electron charge, r_e is the classical radius of the electron, and c is the speed of light [5]. The expression is independent of electric and magnetic field distribution and the presence of charged particles. The last factor represents a relativistic correction. Further details on magnetic deflection of ions crossing the gap and detailed notes about operation of the applied magnetic field diode can be found in [5] and the references therein.

1.3   Pinch-Reflex Diode

PRD operation begins with electrons emitted from a cathode that undergoes large electric field stress. These electrons cross the AK gap and the current generated by
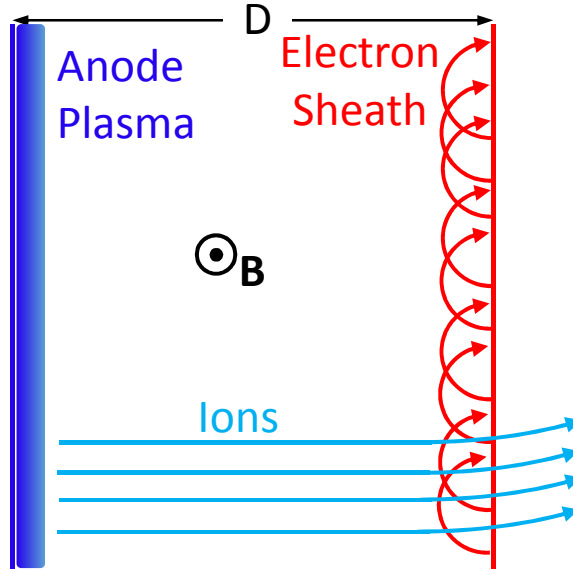
Figure 1.1: A simple diagram showing an applied magnetic field ion diode geometry. The anode conductor is shown in blue and the cathode conductor is shown in red. The anode plasma that serves as the ion source and the electron sheath are also shown. The applied magnetic field is pointing out of the page.

this flow creates an azimuthal magnetic field that in turn causes the electron motion to bend radially in toward the center of the diode. The critical current in the PRD occurs when the electron Larmor radius (nonrelativistic: $r_L = v_e/\omega_c = \sqrt{2Km_e}/eB$, where v_e is the electron velocity, ω_c is the electron cyclotron frequency, and K is the kinetic energy of the electron) equals the AK gap. When critical current is achieved, the electron beam travels very near the anode and creates an anode plasma. Electrons rapidly move toward the center of the diode due to the anode plasma ion space charge. The PRD has a large aspect ratio, defined as the diode radius (R) divided by the AK gap (D). Ion production is enhanced by having a large electron path length, approximately R, compared to the ion path length, approximately D. In addition to the large R to D ratio created by the geometric configuration, the PRD further increases the electron path length with a thin anode foil that allows electron reflexing. The magnetic field created by the return current through the anode results in the reflexing of the electrons multiple times as they move radially inward. A simple diagram of a PRD showing electron reflexing can be found in Fig. 1.2.
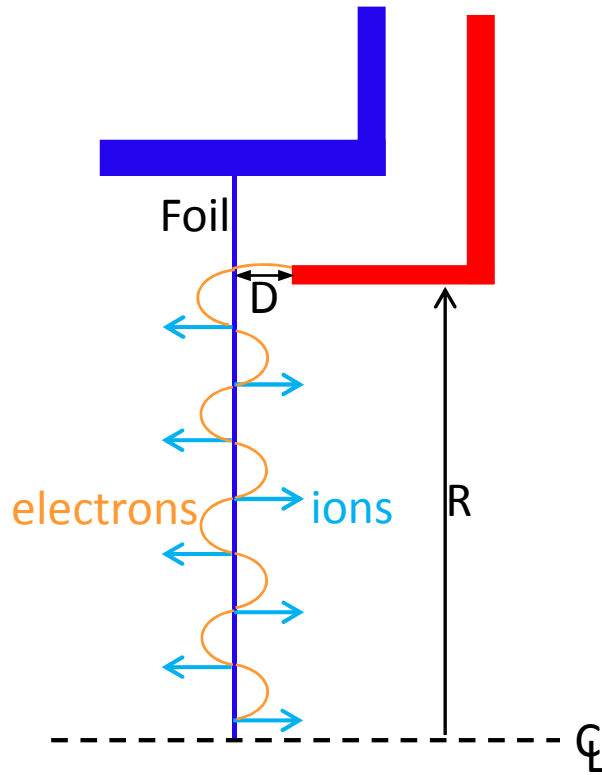
Figure 1.2: A diagram in the r-z plane of a PRD geometry is shown. Also depicted are electrons reflexing through the anode foil, ions being emitted from the anode foil, and relevant diode parameters R, the cathode radius, and D, the AK gap. Anode electrodes are shown in blue and cathode electrodes are shown in red.

PRDs can have anode foils that are either planar, as depicted in Fig. 1.2, or curved, the latter of which is referred to as a focusing PRD. In the focusing PRD, the anode foil and backing plate form a spherically curved section [6].

The anode foil must be sufficiently transparent to electrons such that they can pass through it without being completely stopped. When the diode receives a high-voltage pulse, the electrons emitted by the cathode move toward the anode foil. At the foil the electrons pass through, sometimes oscillating back and forth through multiple times, where their deposited energy heats the anode foil. Oscillation of the electrons through the foil occurs when the electrons encounter the electric fields created by the potential difference between the anode, the cathode, and a virtual cathode which is formed by the oscillating electrons downstream of the anode foil.

This heating results in the formation of a surface plasma which is the source of ions in the system. The ions are emitted perpendicular to the anode plasma [6].

Ion production efficiencies of the PRD are determined by the ratio of ion current to total current. The diode impedance, Z, is proportional to D/R. Since the ion beam current is enhanced with increasing aspect ratio, lower diode impedances generally mean improved diode performance. Predictions of PRD impedance can be obtained using the equation given by [7]

$$Z_D = \alpha(V_D) \left(\frac{V_D}{V_D + \frac{2m_e c^2}{e}} \right)^{1/2} \frac{D}{R},$$ (1.3)

where $\alpha(V_D)$ is a scaling factor in Ω.

The PRD has been used on high current, high voltage, pulsed-power generators including but not limited to Gamble II [8], PITHON [6], AURORA [6], Reiden IV [4, 9], Mercury [7], and Hydra [10]. Ion species in PRDs developed for ICF purposes range from protons to carbon ions. Given the different ion masses, the diodes must operate across many voltages and impedances, ranging from 2-8 MV and 1-10 Ω [6].

As mentioned above, the impedance behavior of the PRD limits the overall diode performance. Several explanations for the impedance collapse in the PRD have been offered and show varying levels of agreement with experimental data, but none have been conclusively proven and the cause(s) of impedance collapse in the PRD is still unknown. Two of these theories involve plasma gap closure and charge-exchange neutrals in the AK gap.

1.3.1   Plasma Gap Closure

Some studies have investigated anode-plasma dynamics in PRDs [6, 11, 12, 13, 14]. One study using a ruby laser interferometric holography system found uniform plasma expansion until just before peak power. After peak power anode plasma expansion showed high velocity, up to 30 cm/μs. During the pulse collapse a high density ($n > 10^{18}$/cm^3) plasma bridged the AK gap [6]. Maenchen found that closure

velocities up to 30 cm/μs were observed late in the pulse and occurred preferentially near the axis of symmetry [12]. This corresponds to a thermal expansion of 0.4 keV CH_2 plasma which is not possible from Ohmic heating alone for the given parameters [15]. Similarly, Nardi, Peleg, and Zinamon [13] have shown that 10 cm/μs expansion occurs near the anode center due to electron energy deposition [15].

Colombant used a 1D magnetohydrodynamic (MHD) model to explore anode-plasma expansion. Early time thermal expansion exists and $\vec{j} \times \vec{B}$ forces slow the front. It is also responsible for accelerating most of the anode plasma to large velocities, up to tens of cm/μs. These results suggest that there is a lower limit to both the size for high-power diodes and the pulse length to prevent limitations and losses from anode-plasma gap closure. This study found that the large final velocities of the anode plasma and the occurrence near the axis of symmetry were reproducible by the MHD model. The anode material here is polyethylene, and therefore nonconducting with a C_2H_4 plasma [15].

Prono used a framing camera to look at the AK gap in a PRD. Results suggest that neither anode nor cathode plasma expansion are dominant causes of gap closure. Light recorded from plasma expansion on both sides of the AK gap showed that expansion was slower than the gap closure observed in the experiment. Beyond the light seen from the electrode plasma, the camera captured a column of light that appeared uniformly between the two expanding plasmas before AK gap closure [14]. Typical cathode plasma expansion occurs at a rate of 2 cm/μs [7]. Anode plasma expansion rates are roughly 1 cm/μs [16].

1.3.2   Charge Exchange Neutrals

Several studies have found that the impedance collapse behavior of the PRD cannot be explained entirely by plasma gap closure. The idea of charge-exchange neutrals filling the AK gap was first presented by Prono in 1981 [14]. In the PRD, when electrons emitted from the cathode surface cross the AK gap and strike the anode foil, depositing energy in it, an anode plasma is formed. This plasma is partially

ionized [14] and results in the formation of a layer of neutrals near the anode surface. A potential gradient is created inside the plasma along which ions move. This motion carries the ions through the neutrals where it is possible for an energetic (moving) ion to collide with a slow or stationary neutral. In the collision, an electron is exchanged between the slow neutral and the fast ion and results in an energetic neutral and slow (effectively zero energy) ion. A diagram of the charge exchange collision principle is shown in Fig. 1.3. In the PRD, these newly created energetic neutrals have energy less than 10 keV [14] and move out of the plasma and into the AK gap. Since a single ion can create multiple fast neutrals, having a higher neutral flux than ion flux from the plasma is reasonable [17]. Charge exchange in the PRD is depicted in Fig. 1.4.
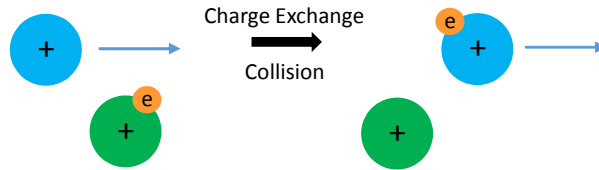
Figure 1.3: When an energetic ion strikes a slow neutral, an electron is exchanged between the two atoms (charge exchange) resulting in an energetic neutral and a slow ion.

Prono presented experimental evidence of the presence of charge-exchange neutrals in a PRD's AK gap. In the study, a framing camera was used on a PRD with a 1 μs pulse [14]. The framing camera captured light emission from a dim column between the anode and cathode plasmas. It intensified just before and after the AK gap was shorted but never reached the intensity of light emitted from the dense plasmas on either side of it. This led to the theory that neutrals were present in the gap and were ionized by the ion and electron beams present in the diode. The analytic model proposed in Ref. [14] gives an estimate of neutral density present for PRD operation requirements as 10^{16}-10^{17} cm^{-3} and the neutral flux is estimated to exceed the ion flux by more than a factor of 10. In this model reionization of energetic neutrals by ions is ignored since the neutral to ion density ratio is so large (up to 100:1). Also omitted from the model is interaction of energetic particles with the background gas. This model suggests that ion energy distribution is degraded when

energetic neutrals are created. Prono suggested anode preionization as a possible technique to minimize or eliminate energetic neutral creation [14].

1.4   Organization of this Thesis

This Thesis presents the results of computer simulations of a PRD using the particle-in-cell (PIC) code Lsp[18]. Chapter 2 discusses the simulation model geometry and particle creation techniques utilized in the simulations. Chapter 3 presents the simulation results for cathode plasma and charge exchange simultions. The results are summarized and discussed in Chapter 4.
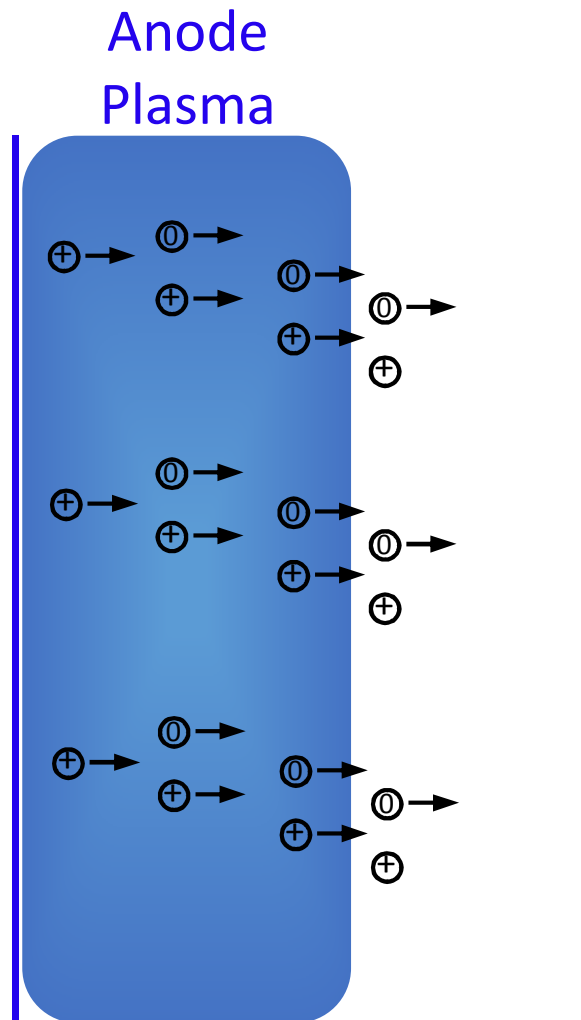
Figure 1.4: An AK gap with a weakly ionized anode plasma where charge exchange occurs, sending energetic neutrals into the vacuum gap. The energetic neutrals in the AK gap are less than 10 keV.

Chapter 2

Simulation Model

2.1 Model Overview

The geometry used for the simulations discussed here is based on the PRD fielded on the Mercury accelerator at the Naval Research Laboratory (NRL) in Washington, DC, as described in [7]. The PIC code Lspis used to carry out fully kinetic, electromagnetic (EM), relativisitic, 2D-cylindrical simulations of the PRD. The 2D-cylindrical geometry extends 10 cm in radius and from -6 cm$< z < 7$ cm, as seen in Fig. 2.1. A 2.03 cm AK gap (D) is present between the cathode (red) blade and anode (blue) foil. The cathode blade is at a radius (R) of 6 cm. These diode parameters are consistent with nominal diode operation of 3.5 MV and 325 kA [7].

The simulation grid is comprised of non-uniform cells that range in size along each side from 0.0101 cm to 0.0399 cm. The smallest dimension is always perpendicular to the emitting electrode surface. The gridding along the anode foil is shown in Fig. 2.2. The time step Δt is set to $4.717 * 10^{-5}$ ns to resolve both the electron-cyclotron (ω_{ce}) and electron-plasma (ω_{pe}) frequencies to satisfy the Courant-Friedrichs-Lewy condition [19], $\omega_{ce}, \omega_{pe} \Delta t < 2$.

The model is driven at the simulation boundary at r=10 cm, 0.85 cm$< z <$3.02 cm by a forward-traveling voltage waveform with a 5 ns rise from zero to 3.0778 MV,
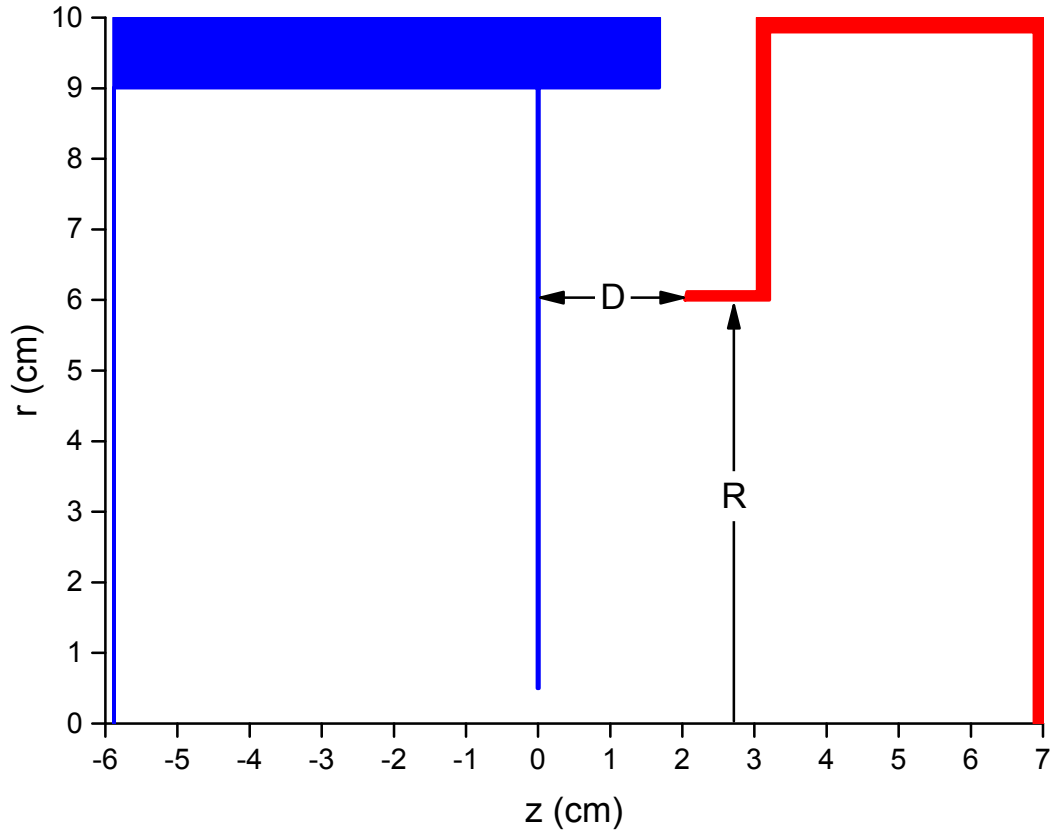
Figure 2.1: The 2D-cylindrical geometry used for the LsPsimulations. Cathodes are shown in red and anodes are shown in blue. The anode foil is centered at Z=0.

as seen in Fig. 2.3. This voltage was chosen to yield a diode voltage of roughly 3.5 MV that is representative of the peak voltage during normal diode operation. The simulations were run for 20 ns to allow for ringing in the system to dissipate and to clearly determine operating power. Utilizing a rapid rise-time drive pulse results in notably shorter simulation run time in comparison to the 60 ns rise time of a realistic voltage pulse. The simulation results shown here are idealized and are representative of experimental peak values but not experimental pulse-shapes.

Foils used in PRD experiments are typically on the order of 10 microns thick, within an order of magnitude. Creating grid cells small enough to resolve such a foil is not practical for the PRD geometry. The anode foil in the simulations is represented by a 2-cell (0.02 cm) thick conductor that has analytic approximations for scattering and energy loss in carbon.

Figure 2.2: An example of the nonuniform gridding near the anode foil (blue line on left) in the PRD simulation. The smallest dimension is 0.0101 cm and the largest dimension is 0.0399 cm.

2.2   Particle Creation

Particle creation in the simulation space is accomplished using 6 different models. A space-charge-limited (SCL) emission algorithm is used for cathode-electrons emitted due to field-stress on cathode electrode surfaces. A secondary emission model is used for electrons emitted from the anode foil as impacting electrons emitted from the cathode strike the anode foil. Ion emission from the anode foil is accomplished with another space-charge-limited emission algorithm. The electrode desorption and particle fragmentation models work together to create the plasma formed at cathode surfaces. A simple creation model is used to lay down static neutrals for the charge exchange model.
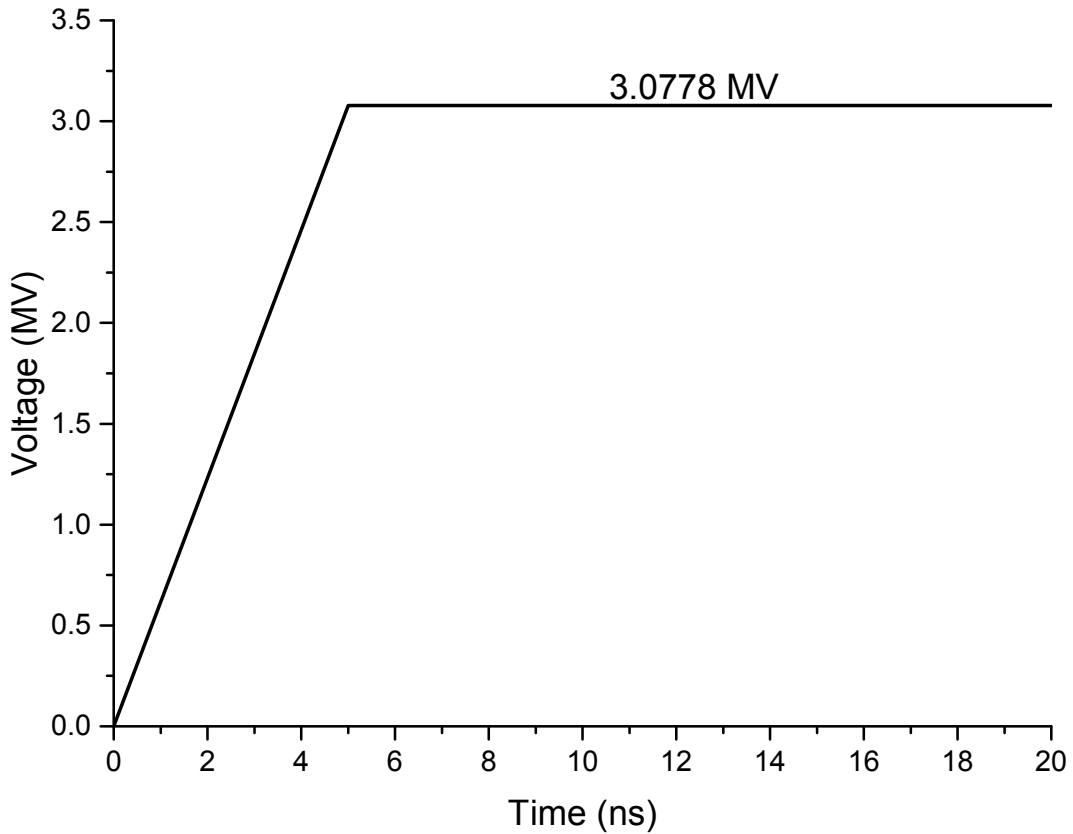
Figure 2.3:   The voltage pulse used to drive the PRD simulation at the r=10 cm boundary.

2.2.1   Space-Charge-Limited Emission Model

Emission of space-charge-limited electrons from cathode surfaces that undergo a field-stress of 240 kV/cm is enabled along the cathode blade in the area enclosed by the green dashed line in Fig. 2.4. The 240 kV/cm threshold is a generally accepted value for stainless steel conductors [20].

2.2.2   Anode Ion Emission Model

Plasma formation along the anode foil in the PRD can be contributed to by both Ohmic heating and heating due to electron bombardment. Ions can be accelerated out of this plasma. In this simulation model, SCL ion emission is enabled along the anode foil when the surface temperature exceeds 5 K. This is an artificially
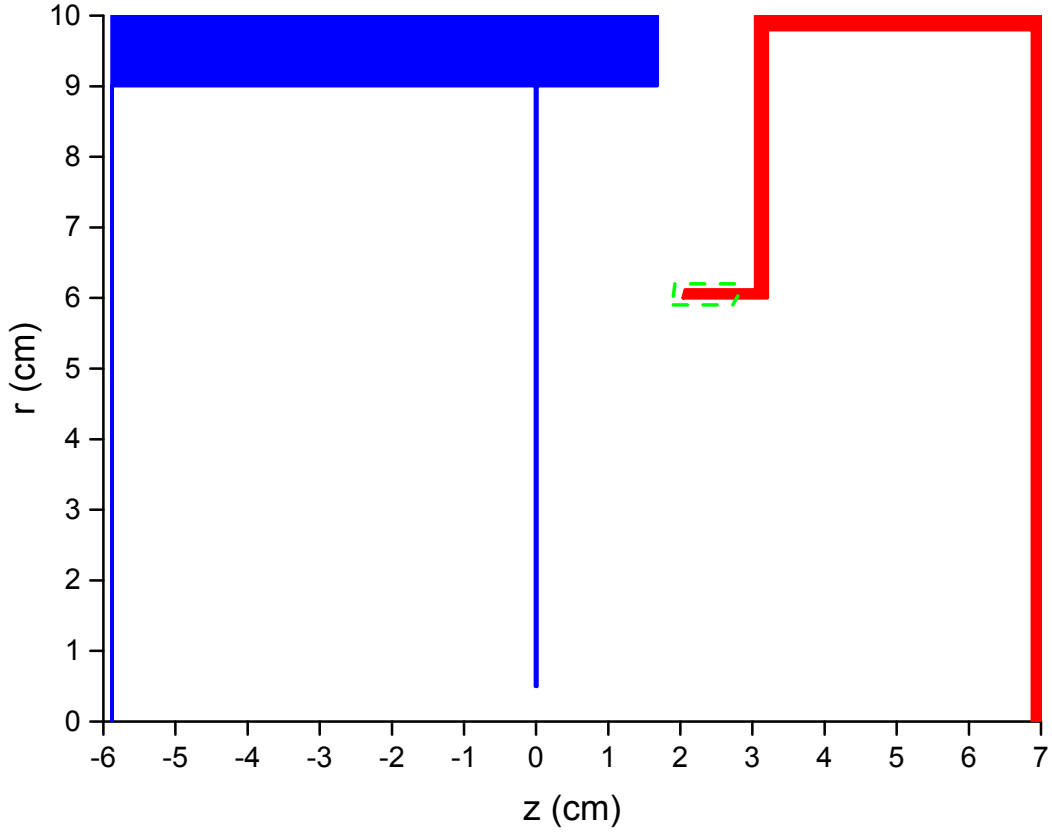
Figure 2.4: SCL emission of electrons is enabled from the cathode blade surfaces in the area enclosed by the green dashed line.

low temperature threshold chosen to ensure rapid ion production in the simulation. The purple dashed line in Fig. 2.5 shows the enabled ion emission region. Electron energy deposition and Ohmic current conduction rapidly heat anode surfaces, leading to dense surface plasma formation. Ions are subsequently accelerated from these thin, high-density anode plasmas. The model assumes SCL emission of ions directly from surfaces for which the local temperature has increased by a designated amount.

2.2.3   Secondary Emission Model

The secondary emission model in LSPis used along the anode foil of the PRD simulation model in the same region as the anode ion emission, see Fig. 2.5. This model
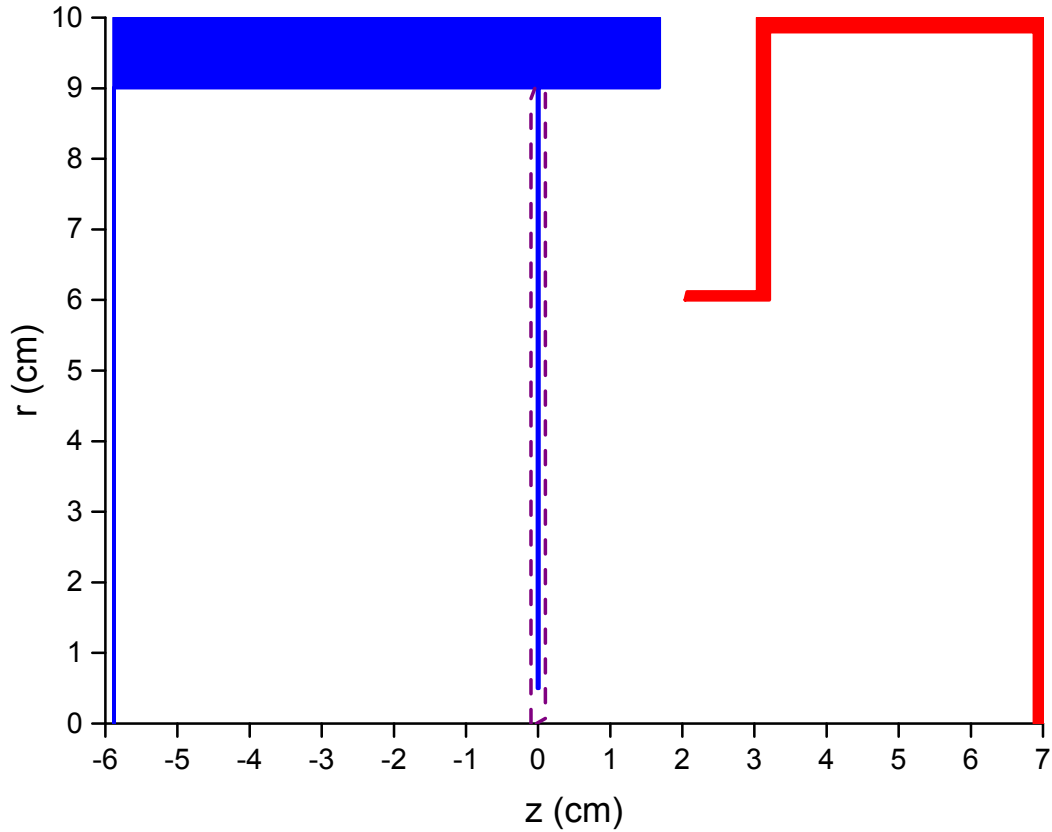
Figure 2.5: SCL ion emission and secondary emission of electrons are enabled from the anode foil surfaces in the area enclosed by the purple dashed line.

mimics the emission of secondary electrons on a foil that is being bombarded by an electron beam. Electron emission is allowed every time-step.

2.2.4 Desorption and Fragmentation Models

Cathode plasma creation in the simulation assumes the explosive emission of electrons and the desorption of a neutral, thermal particle layer from the electrode surface at a prescribed rate. Desorption of neutrals is determined for each individual cell along the conductor where the electric field exceeds the threshold value of 240 kV/cm. These neutrals are then split into electron-ion pairs which serve to form the cathode plasma. The desorption and fragmentation regions in the PRD simulation are outlined in the red and blue dashed lines, respectively, in Fig. 2.6.
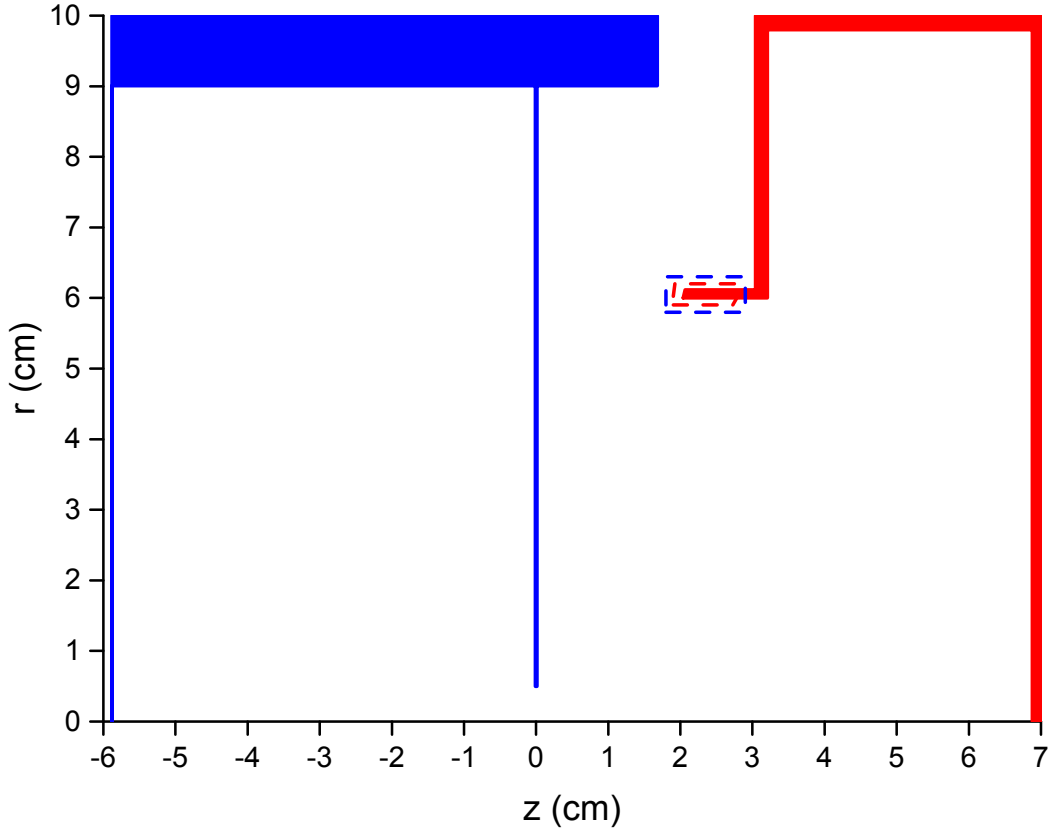
Figure 2.6: Desorption of neutral particles is enabled from the cathode surfaces in the area enclosed by the red dashed line. Fragmentation of these neutral particles into ions and electrons is prescribed in the area enclosed by the blue dashed line.

2.2.5   Charge Exchange Model

Charge exchange in LSPis treated as a momentum-transfer event between a neutral and charged particle of the same species. The momentum-transfer frequency due to charge exchange for hydrogen is shown in Fig. 2.7. For the collisions utilized in these simulations, momentum-transfer due to scattering is ignored and only charge-exhcange momentum transfer is considered.

A 0.4 cm thick layer of stationary neutral H_2 particles is created along the anode foil across from the cathode blade, as shown in Fig. 2.8. The neutral density is set at $5 * 10^{16}$ cm^{-3}, the average density used by Pointon in his one-dimensional simulations for charge exhcange in an ion diode [17].
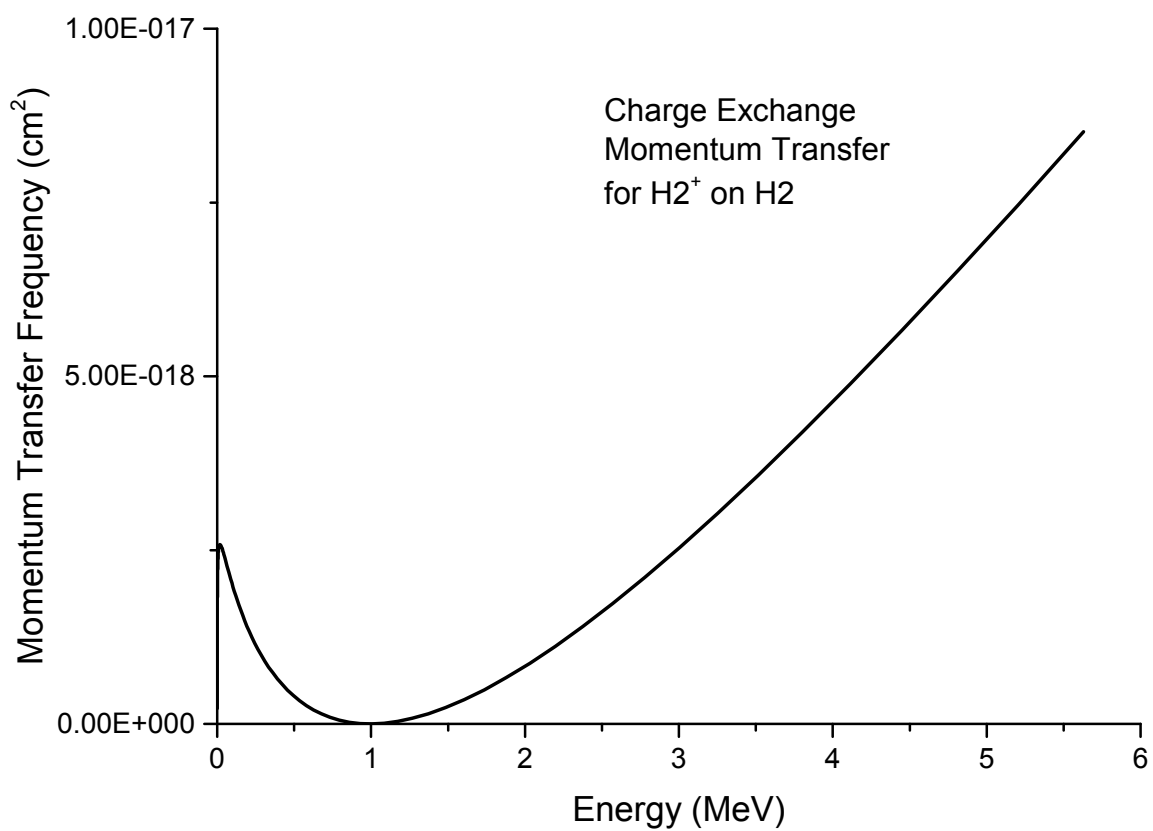
Figure 2.7: The momentum-transfer frequency due to charge exchange for H_2^+ on H_2 neutrals.
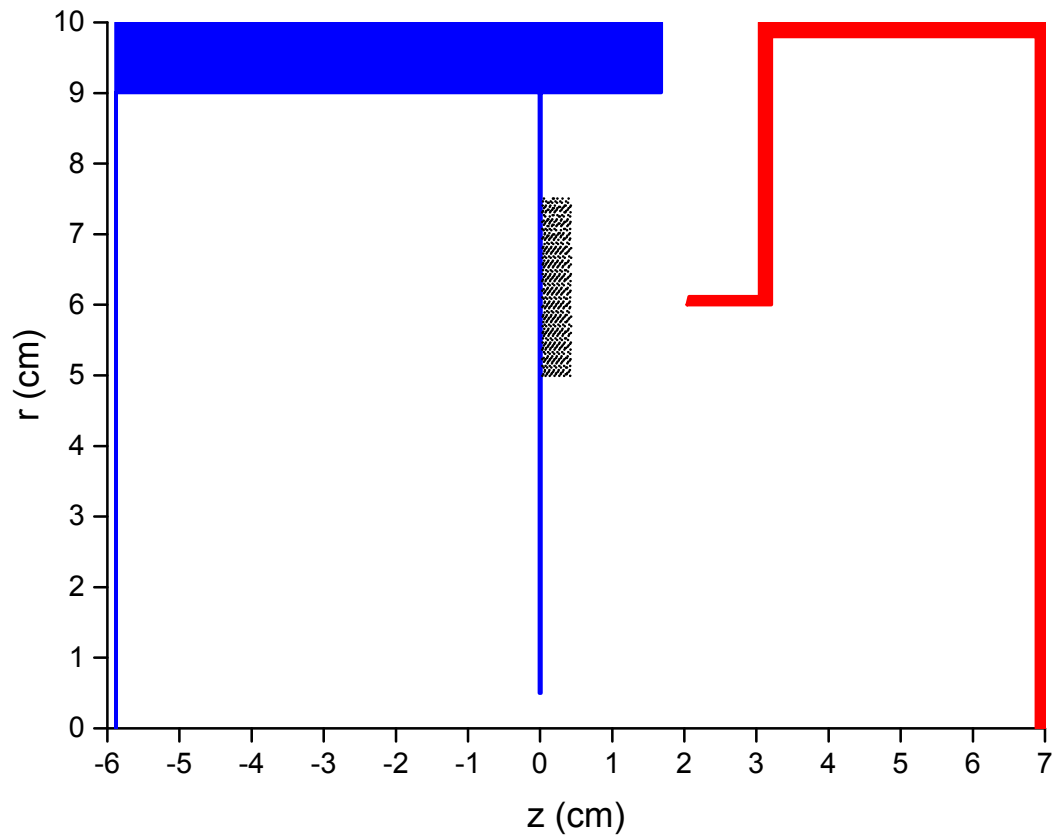
Figure 2.8: Neutral H_2 particles are created in a 0.4 cm thick band with a density of $5 * 10^{16}$ cm^{-3} in front of the anode foil in the PRD simulation.

Chapter 3

Simulation Results

3.1 Baseline Simulation Results

The simplest simulation conducted involved SCL electron emission from the cathode blade, proton emission from the anode foil, and secondary electron emission from the anode foil. This simulation is treated as the baseline simulation to which all other variations can be compared. It yields a diode current of 328.2 kA and diode voltage of 3.51 MV, resulting in a diode impedance of 10.7 Ω, in excellent agreement with the predicted diode impedance of 10.7 Ω that is calculated by

$$Z_D = \frac{V_D}{I_A} = \alpha(V) \left(\frac{V_D}{V_D + \frac{2mc^2}{e}} \right)^{1/2} \frac{D}{R}, \tag{3.1}$$

where α is a scaling factor expressed in Ω, here 36 Ω, V_D is the diode voltage, m is the electron mass in kg, c is the speed of light, e is the electron charge in Coulombs, D is the AK gap in cm, and R is the cathode blade radius in cm [7]. Time histories of this data are shown in Fig. 3.1.

The ion current produced was 74.7 kA, again in excellent agreement with the theoretically predicted value of 76.4 kA calculated by

$$\frac{I_{ion}}{I_e} = \eta(V) \sqrt{\frac{m}{M}} \sqrt{\frac{\gamma + 1}{2}} \frac{R}{D}, \tag{3.2}$$
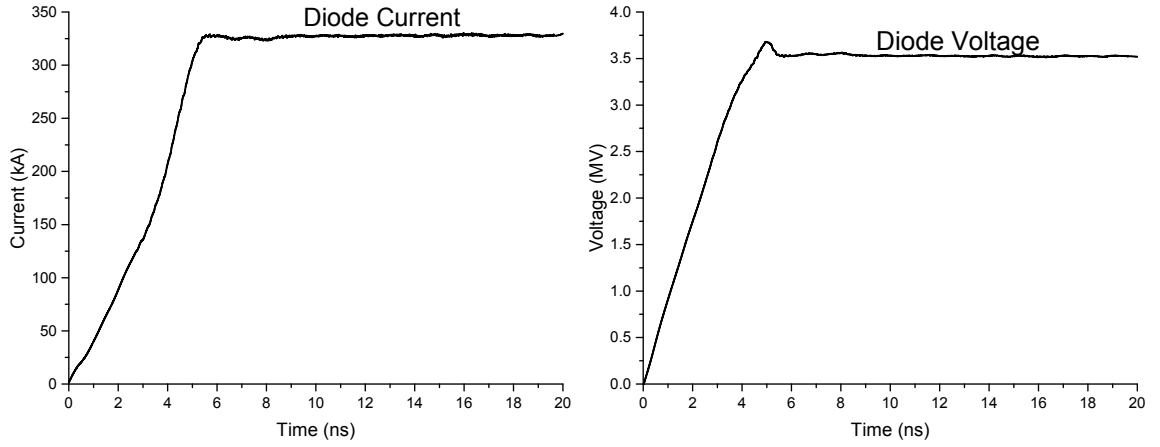
Figure 3.1: The left frame shows the diode current and the right frame shows the diode voltage for the baseline PRD simulation. The diode operates at the predicted value of 10.7 Ω.

where η is a predetermined constant, here 1.62 [7].

Electron density plots show electrons streaming from the cathode blade and striking the anode foil. Ion density plots show higher density on axis, where the ion beam is formed. Both of these density plots can be seen in Fig. 3.2

3.2   Cathode Plasma Simulation Results

3.2.1   Plasma Desorption Rate

Having established the overall behavior of the simulation model as compared to experimental diode behavior, the cathode plasma creation model described earlier was included in the simulation. The neutral desorption rate, R_{desorp}, of $7.5 * 10^{-3}$ ml/ns was the starting point for cathode plasma desorption. Each monolayer (ml) is equal to 10^{15} cm^{-2}. This value is in the typical range of containment desorption rates in pulsed-power vacuum environments [21].

In this cathode plasma simulation the diode voltage and current are nearly identical to baseline values and the ion current is unchanged. Ion density near the cathode
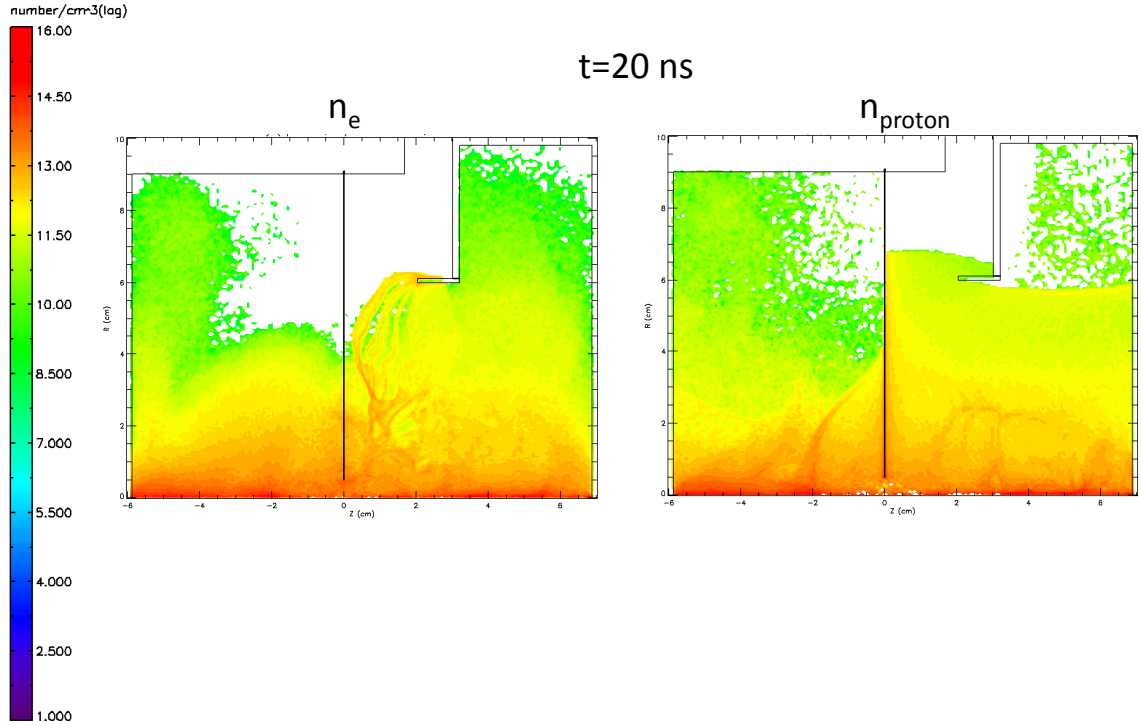
Figure 3.2: The left frame shows the electron density in the baseline PRD simulation. The right frame shows proton density. Electrons streaming from the cathode blade and higher ion density on-axis show that the simulation behavior mirrors that of experiments.

is compared for the baseline simulation and the plasma simulation at t=20 ns in Fig. 3.3. Note that no appreciable plasma accumulation in the AK gap is observed, suggesting that cathode plasma formation is not the primary mechanism responsible for PRD gap closure.

The plasma desorption rate was increased to test the effects on AK gap closure. Simulations were performed for $R_{desorp} = 1.5 * 10^{-2}$ ml/ns and $R_{desorp} = 2.25 * 10^{-2}$ ml/ns. Simulation time histories of the three plasma cases compared with the baseline case are presented in Fig. 3.5. Of the three values tested here, desorption rate of the cathode plasma appears to have negligible effects on PRD operation. Similarly, no notable AK gap closure is seen, with ion densities shown in Fig. 3.4. Increased ion density can be seen on the inner-radius of the cathode blade but after 20 ns of simulation time the high density has not expanded away from the conductor surface.
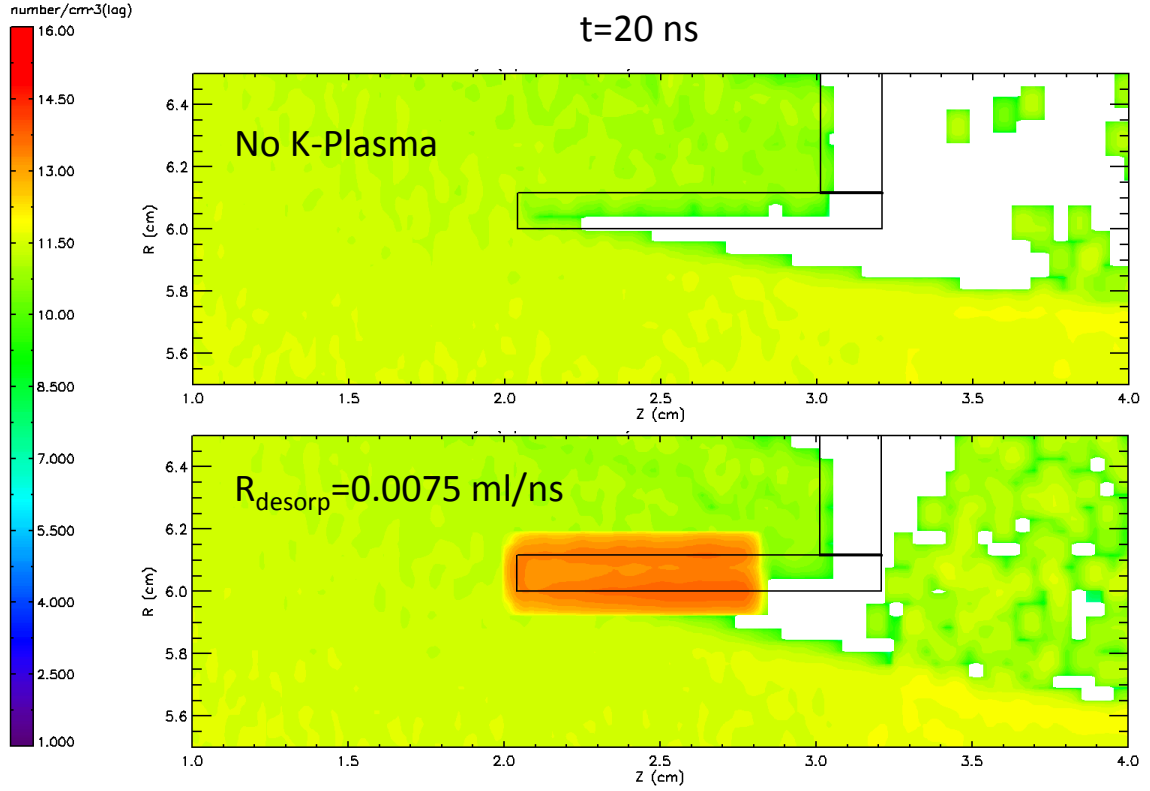
Figure 3.3:   The top frame shows ion density in the baseline PRD simulation and the bottom frame shows ion density in the plasma simulation. No notable accumulation of plasma ions can be seen extending into the AK gap.

3.2.2   Ion Species

The baseline simulation and the three plasma simulations presented thus far all utilized protons for the ion species. In an experimental facility, different ion species are expected to be found, such as hydrogen and carbon, depending on the thin anode material[22]. Also, the low pressure conditions of the experimental facility are not a perfect vacuum, so some surface contaminants and gas particles can be expected. Four additional species, H_2, N_2, H_2O, and C, were tested to simulate the presence of these contaminants. The simulations include only the first charge state for these ion species. In experimental settings, higher charge states can and do occur [23], but testing the impact of multiple charge states for multiple species is beyond the scope of this work.
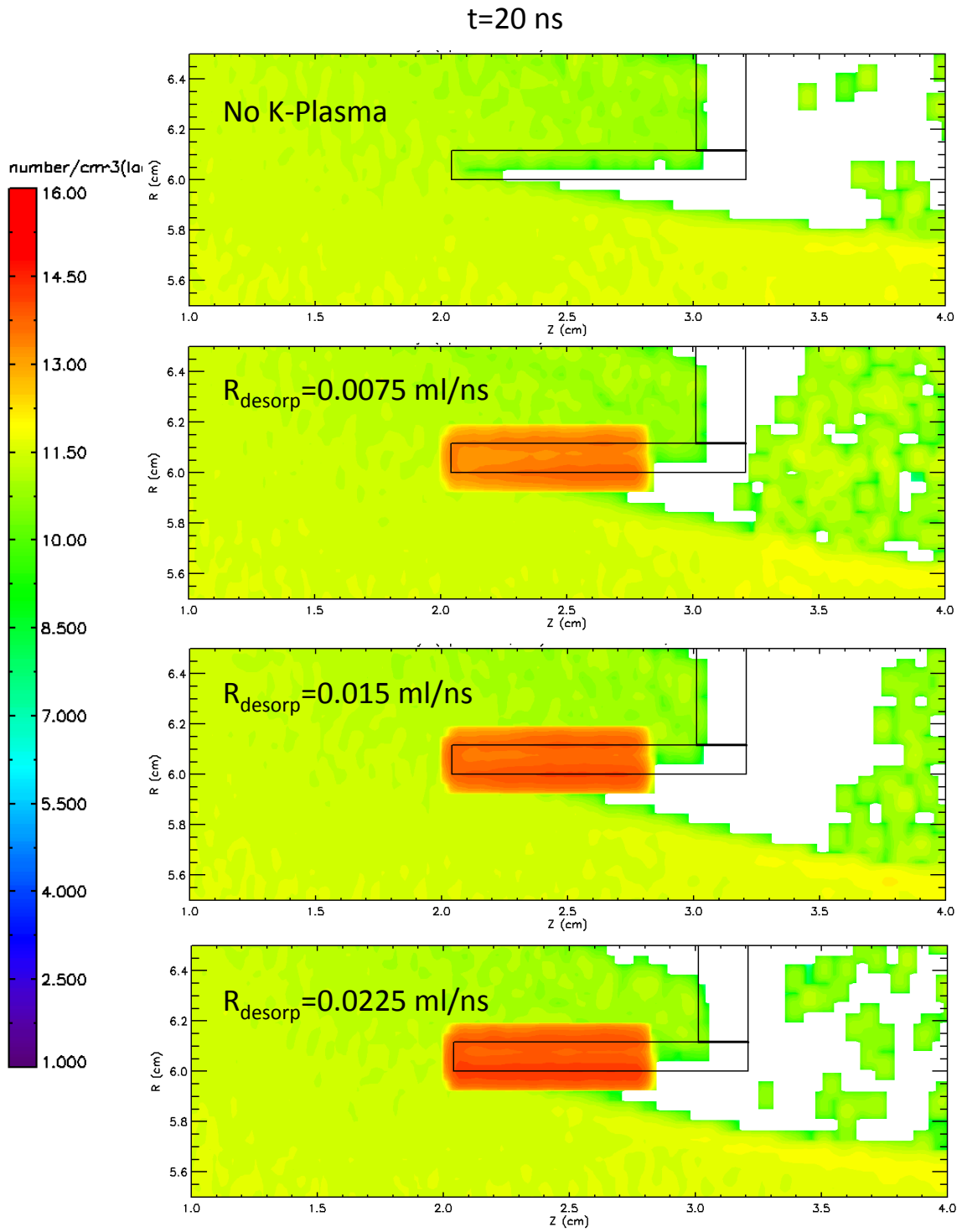
Figure 3.4: Plasma ion density comparison for four desoption rates, R_{desorp}=0, $7.5*10^{-3}$, $1.5*10^{-2}$, and $2.25*10^{-2}$ ml/ns.
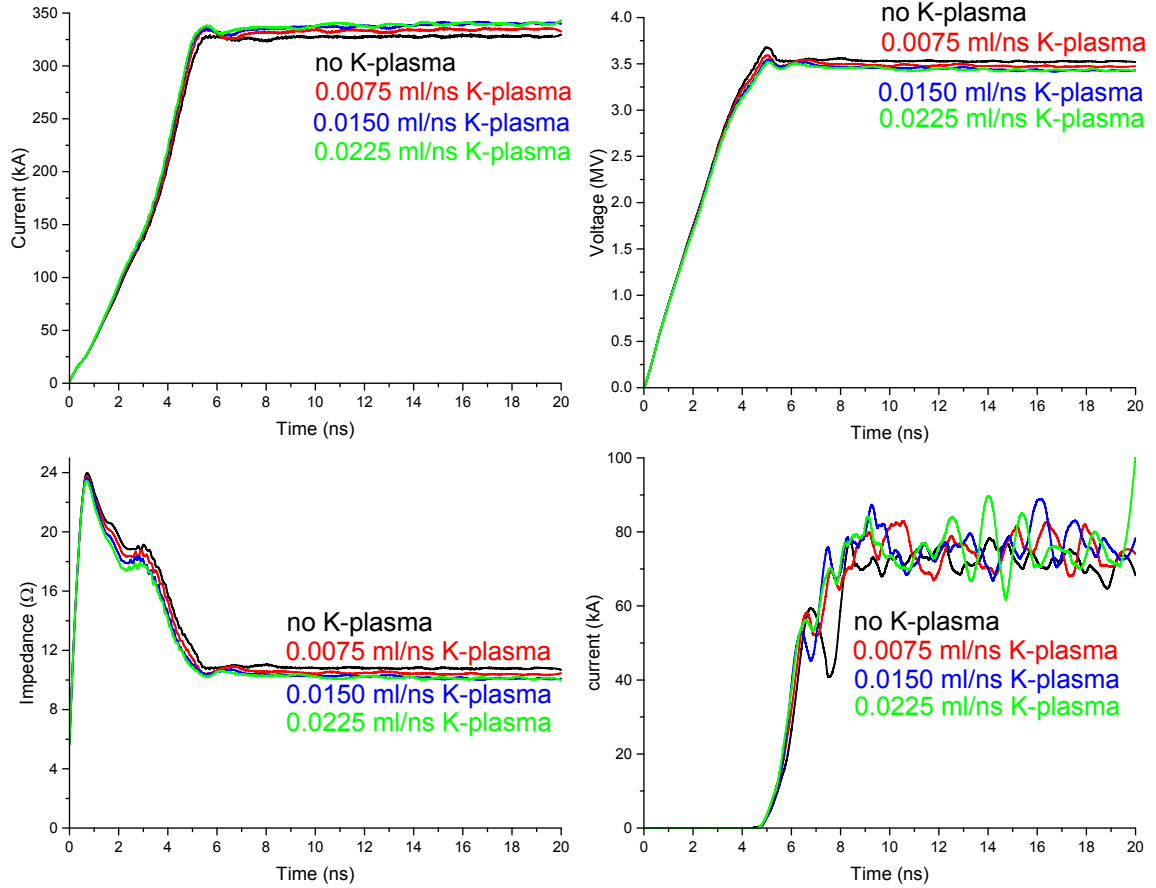
Figure 3.5: Diode current is seen in the upper left frame. Diode voltage is in the upper right frame. The lower left frame depicts diode impedance and the lower right frame depicts proton current. All plots show the baseline data (black line), R_{desorp}=0.0075 ml/ns data (red line), R_{desorp}=0.015 ml/ns data (blue line), and R_{desorp}=0.0225 ml/ns data (green line).

The H_2 simulation has diode voltage and current that are nearly identical to the proton simulation. Despite the ion current, 59 kA, being 15 kA lower than the proton case, it is in good agreement with the theory prediction of 54 kA from Eq. 3.2.

The N_2, H_2O, and C simulations all have a different wave shape than that seen in the proton and H_2 simulations. The diode voltage and current take 13, 11, and 9 ns, respectively, to stabilize, as opposed to the 6 ns seen in the H_2 and proton cases. These heavier ion simulations also exhibit a lower dZ/dt than their lighter counterparts. Again, ion currents in these cases, 13 kA (N_2), 18 kA (H_2O), and 22 kA (C) are in excellent agreement with theoretical predictions of 14, 18, and

22 kA, respectively. As seen in the diode voltage and current, the ion current rises later and more slowly than the lighter ion simulations. Time histories for the diode current, diode voltage, diode impedance, and ion current are shown in Fig. 3.6.
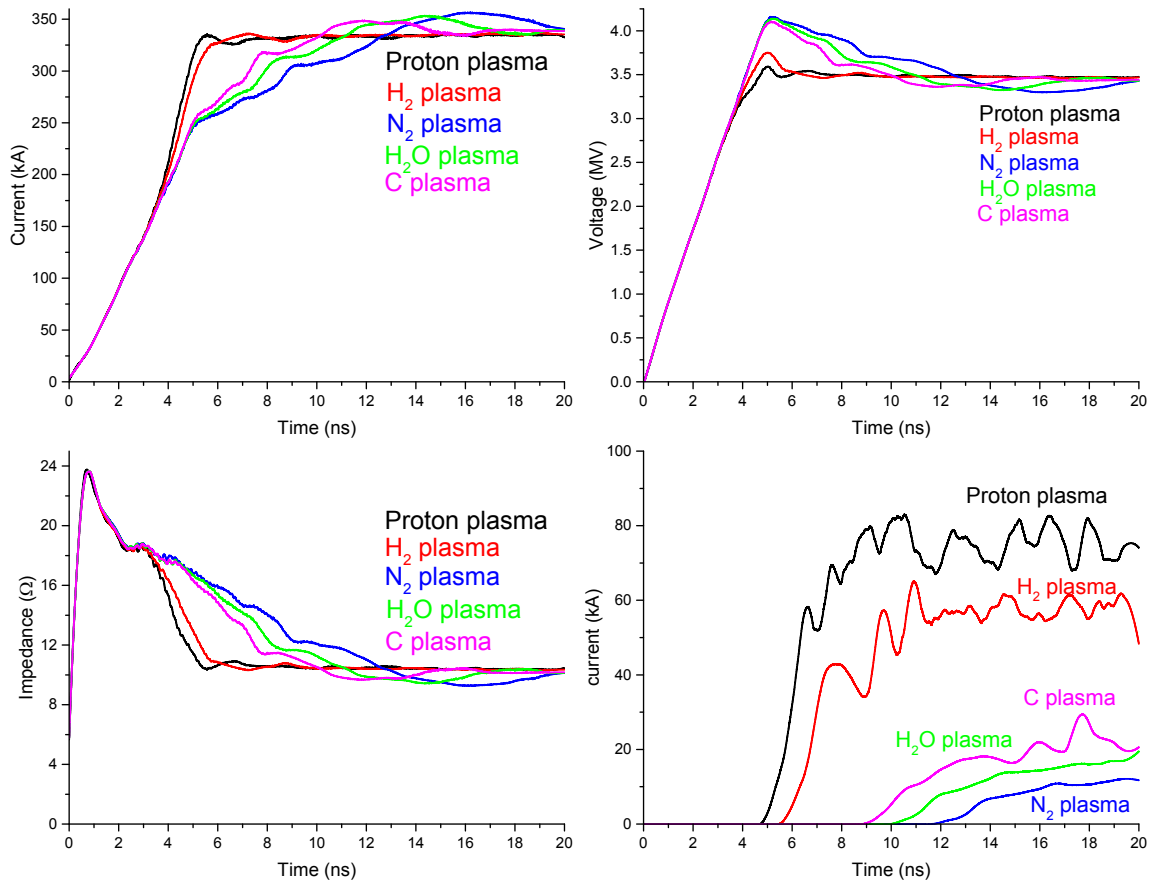
Figure 3.6: Diode current is seen in the upper left frame. Diode voltage is in the upper right frame. The lower left frame depicts diode impedance and the lower right frame depicts proton current. All plots show proton data (black line), H_2 data (red line), N_2 data (blue line), H_2O data (green line), and C data (pink line).

3.3   Charge Exchange

Building on the simulation including H_2 cathode plasma, charge exchange between H_2 neutrals and H_2^+ ions is included. The charge exchange simulation is run for 60 ns, as that is the approximate time of peak current for a PRD typically fielded on Mercury. The filling of the AK gap is shown by four still frames depicting the

position of neutral particles at $t = 0$, 20, 40, and 60 ns in Fig. 3.7. While some neutrals completely cross the AK gap, after 60 ns of run time the neutral density near the cathode is negligible. Densities of interest are seen less than half-way across the AK gap. A line out of neutral density in the AK gap is shown in Fig. 3.8.
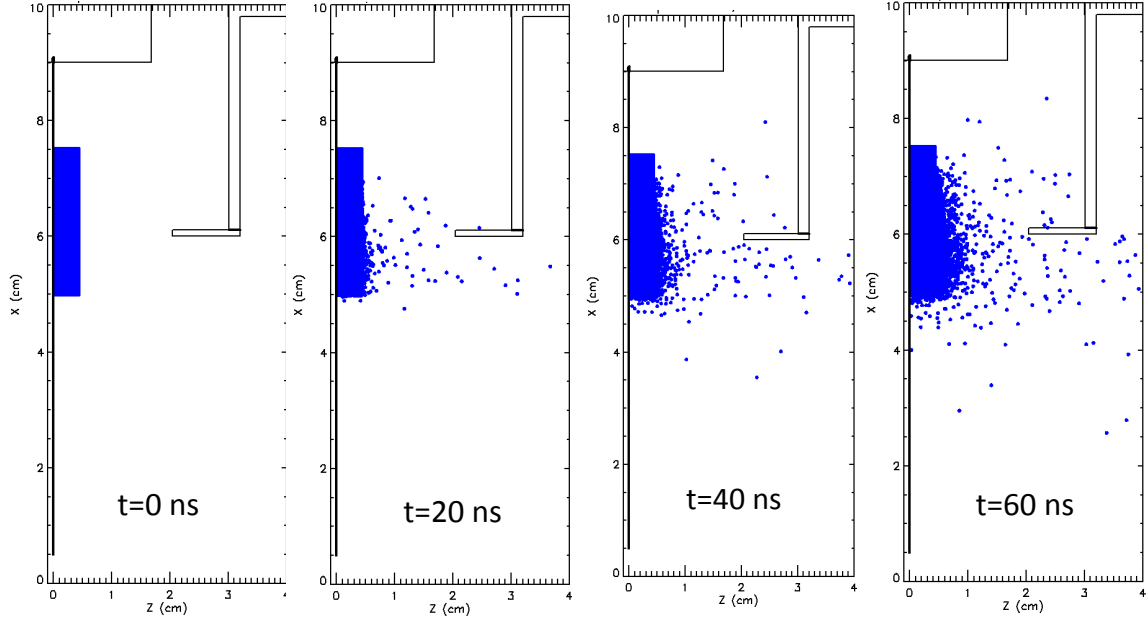
Figure 3.7: Neutrals that have undergone charge exchange fill the AK gap over time. From left to right, neutral position in the AK gap is shown for simulation times $t = 0$, 20, 40, and 60 ns.

The presence of these neutrals in the AK gap of the PRD simulation resulted in minimal changes to the total diode current and voltage. However the ion current was reduced by approximately 14%. Comparisons of the charge exchange time-history data with the H_2 simulation are presented in Fig. 3.9.
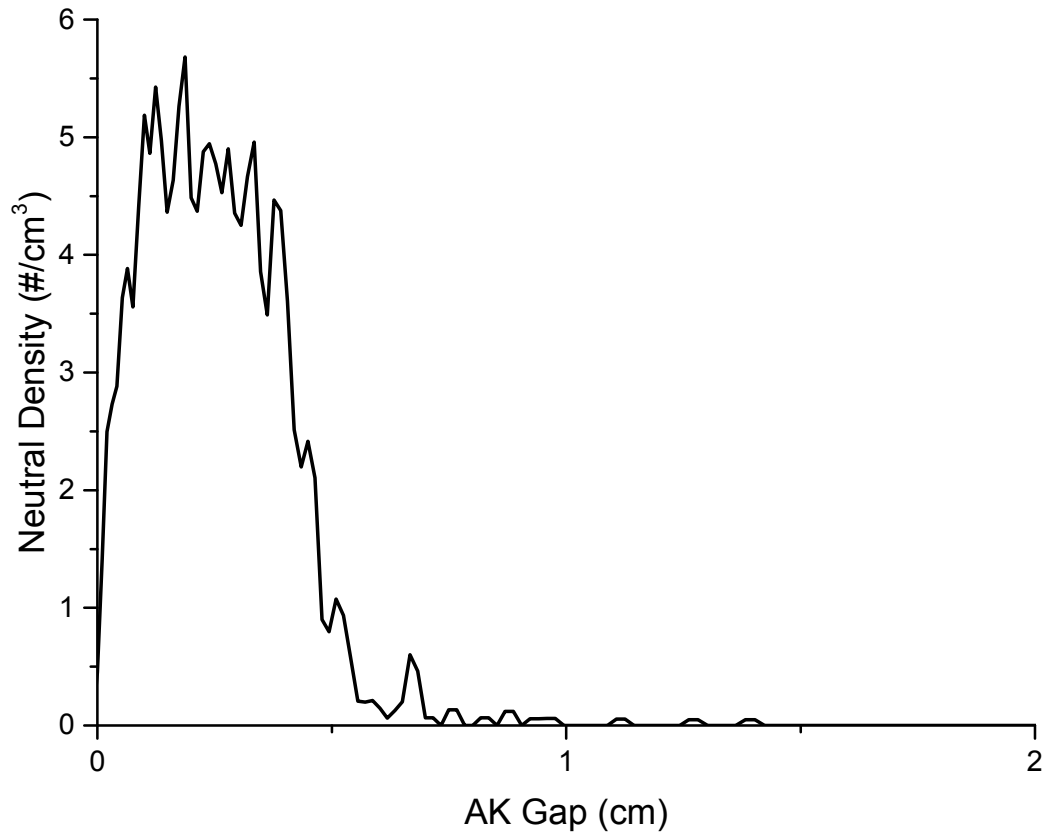
Figure 3.8: Spatial line-out of neutral density at $t = 60$ ns of the charge exchange simulation. The anode foil is at the left side of the plot and the right side is the cathode blade.
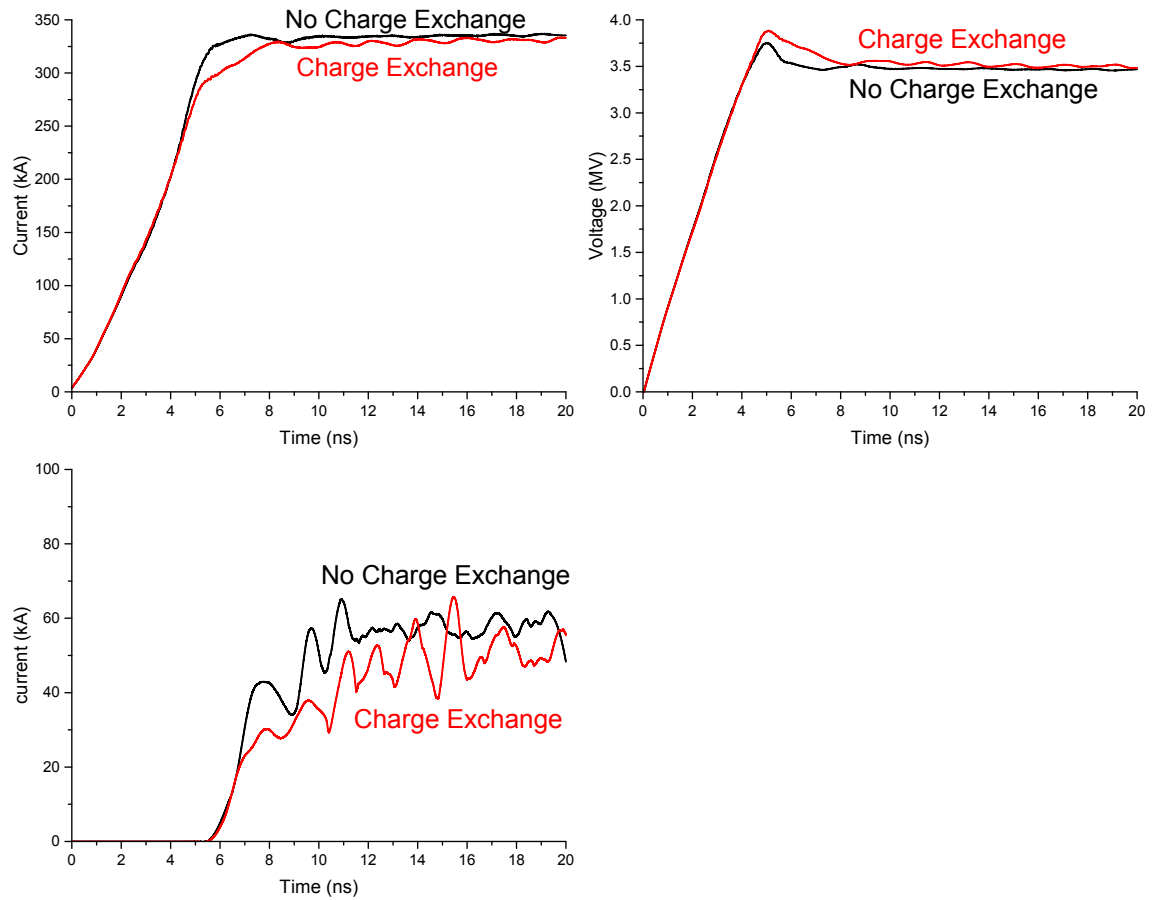
Figure 3.9: Presented here are time-history comparisons for the charge exchange (red lines) and no charge exchange (black lines) simulations. Diode current is seen in the upper left frame, diode voltage is in the upper right frame, and ion current is seen in the bottom frame.

Chapter 4

Summary and Discussion

An idealized 2D, fully kinetic, electromagnetic PIC simulation model of a PRD wtih a planar anode foil has been created. The model is shown to be in good agreement with both theoretical and experimental diode operating values. Several particle creation models were utilzied to study the effects of plasma expansion and charge exchange on the impedance of the PRD.

The inclusion of self-consistent cathode plasma formation with a desorption rate of $7.5 * 10^{-3}$ ml/ns did not have an impact on diode impedance or ion current. Doubling and tripling the desorption rate did not show any further plasma expansion into the AK gap nor any change to diode voltage or currents. Modifications to the ion species from proton to H_2, N_2, H_2O, or C had minimal impact on the diode impedance behavior and showed no additional plasma gap closure. These results are in agreement with previous statements that cathode plasma formation is not the primary mechanism for diode failure in the PRD [12, 14]. These results are for the first charge state for each ion tested. Higher charge state ions present in PRDs are associated with faster growth rates for a given density [23]. Using the lowest charge state in the simulations allowed for the slowest possible plasma growth rate. Had a higher charge state, or a mix of charge states, been used, cathode plasma expansion into the AK gap may have been seen.

While the simulations here study the impact of self-consistent cathode plasma formation, the anode plasma is not able to be studied in the same manner, and similar conclusions cannot be drawn about the impact of anode plamsa formation on diode impednace collapse. Further studies are needed utilizing self-consistent anode plasma formation models.

The effect of charge exchange neutrals filling the AK gap in a relatively short pulse, 60 ns, PRD is small. A neutral density of 10^{16} cm^{-3} fills just under half of the AK gap after 60 ns and causes a 14% decrease in ion current and negligible changes to diode impedance. These findings are in agreement with those of Pointon in his 1-D simulations, that ion current is reduced in the presence of charge exchange, and that neutral density in the AK gap is insufficient for plasma formation in the limit of a 3.5 MV pulse [17]. Both the simulations presented in this Thesis and those discussed in [17] are short-pulse and relatively small AK-gap. The suggestion for charge-exchange being a dominating impedance collapse mechanism is based on a long pulse, 1 μs, with a larger AK gap PRD [14].

Under the idealized assumptions explored here, it is found that for short pulse operation, neither charge exchange neutral filling of the AK gap, nor singly-ionized-cathode plasma expansion into the AK gap contributes to impedance collapse of the PRD.

Further studies are needed to examine long-pulse charge exchange simulations and the effects on PRD impedance collapse. Likewise, examining the effect of charge exchange between different species in short-pulse diodes could be done. These interactions may lead to impedance collapse with faster AK gap filling due to heavier ions colliding with lighter neutrals and more rapid movment of the neutrals.

Appendix: LspInput Deck

The following is the input used in LSP for the Charge exchange simulation described above. It includes all models used from all the simulation variations discussed, but changes to particle species were made for the different cases studied. The particle creation models were included and excluded as needed for the specific mechanism being studied.

```
[Control]
 courant_multiplier 0.2
 time_limit_ns 150.0
 ;number_of_steps 10
;Parallel Processing
 balance_interval_ns 5.0
;Field Solution and Modification
 time_bias_coefficient 0.125
 time_bias_iterations 2
;Particle Collision Algorithm
 scattering_interval 1
;(Diagnostic Output) Flags
 dump_current_density_flag ON
 dump_number_densities_flag ON
 dump_surface_depositions_flag ON
 dump_energy_deposition_flag ON
 dump_rbtheta_current_flag ON
```

```
 dump_rho_background_flag ON

 dump_plasma_quantities_flag ON

;(Diagnostic Output) Dump Intervals

 dump_interval_ns 5.0

 dump_times 1000 10000 end

 probe_interval 5

 scalar_movie_components number_densities

 scalar_movie_interval_ns 0.5

;

restart_interval_ns 1.0

dump_time_zero_flag ON

cold_test_flag OFF

;

;

[Grid]

;

grid1 ; grid 1

rmin              0.0

rmax             10.0

r-cells          287

dr-start 0.01

r-intervals

  length 0.3  for  20  ;  to r = 0.3  cm, dr = 0.020 cm

  length 0.7  for  28  ;  to r = 1.0  cm, dr = 0.030 cm

  length 3.0  for  86  ;  to r = 4.0  cm, dr = 0.0397 cm

  length 2.0  for  51  ;  to r = 6.0  cm, dr = 0.0387 cm

  length 4.0  for 102  ;  to r =10.0  cm, dr = 0.0398 cm

end

;

zmin              -6.0

zmax              7.0
```

```
z-cells             539

dz-start 0.04

z-intervals

  length  4.5  for 150  ; to z = -1.5  cm, ending dz = 0.0200 cm

  length  1.0  for  66  ; to z = -0.5  cm, ending dz = 0.0103 cm

  length  0.5  for  49  ; to z =  0.0  cm, ending dz = 0.0101 cm

  length  0.1  for   9  ; to z =  0.1  cm, ending dz = 0.0121 cm

  length  6.9  for 265  ; to z =  7.0  cm, ending dz = 0.0399 cm

end

;

;

[Regions]

;

region1 ; region 1

;

grid 1

rmin 0.0

rmax 10.0

zmin -6.0

zmax 7.0

number_of_domains 95

split_direction ZSPLIT

number_of_cells AUTO

;

;region2 ; region 2

;;

;grid 1

;rmin 5.0

;rmax 10.0

;zmin -6.0

;zmax 7.0
```

Appendix: LSP Input Deck

```
;number_of_domains 95
;split_direction ZSPLIT
;number_of_cells AUTO
;
;
[Objects]
object1 SOLID
 conductor on medium 0 potential 2
;
object2 CYLINDER ; vacuum upsteam of foil
 conductor off medium 0 potential 0
 base 0.0 -5.9
 polar_angle Z 0.0
 azimuthal_angle X 0.0
 height 16.0
 radius 9.0
;
object3 CYLINDER ; vacuum downstream of anode hardware
 conductor off medium 0 potential 0
 base 0.0 1.67
 polar_angle Z 0.0
 azimuthal_angle X 0.0
 height 10.0
 radius 10.1
;
object4 CYLINDER ; cathode materials
 conductor on medium 0 potential 1
 base 0.0 0.0 3.0
 polar_angle Z 0.0
 azimuthal_angle X 0.0
 height 7.0
```

```
 radius 10.1
;
object5 CYLINDER ; cathode blade (1/2)
 conductor on medium 2 potential 1
 base 0.0 0.0 2.04
 polar_angle Z 0.0
 azimuthal_angle X 0.0
 height 6.0
 radius 6.1
;
object6 CYLINDER ; cathode blade (2/2)
 conductor off medium 0 potential 0
 base 0.0 0.0 1.0
 polar_angle Z 0.0
 azimuthal_angle X 0.0
 height 6.5
 radius 6.0
;
object7 CYLINDER ; vacuum downsrtream of cathode
 conductor off medium 0 potential 0
 base 0.0 3.2
 polar_angle Z 0.0
 azimuthal_angle X 0.0
 height 10.0
 radius 9.8
;
object8 CYLINDER ; foil
 conductor on medium 1 potential 2
 base   0.0 0.0 -0.0105
 polar_angle Z 0.0
 azimuthal_angle X 0.0
```

```
 height 0.0215
 radius 9.1
;
object9 CYLINDER ; cathode ion-beam dump
 conductor on medium 0 potential 1
 base 0.0 0.0 6.9
 polar_angle Z 0.0
 azimuthal_angle X 0.0
 height 1.0
 radius 10.1
;
object10 CYLINDER ; foil hole
 conductor off medium 0 potential 0
 base 0.0 0.0 -1.0
 polar_angle Z 0.0
 azimuthal_angle X 0.0
 height 2.0
 radius 0.5 ;1.0
;
;
[Particle Species]
species1 ; H2_neut
charge 0
mass 3672
atomic_number 1
migrant_species_flag off
implicit_species_flag off
particle_motion_flag on
particle_forces_option AVERAGED
transverse_weighting_flag on
particle_kinematics_option STANDARD
```

```
scattering_flag on

selection_ratio 1

;

species2 ; H2+ ion

charge 1

mass 3671

atomic_number 1

migrant_species_flag off

implicit_species_flag off

particle_motion_flag on

particle_forces_option AVERAGED

transverse_weighting_flag on

particle_kinematics_option STANDARD

scattering_flag on

selection_ratio 1.0

;

species3 ; Cathode AND Plasma Electrons

charge -1.0

mass 1.0

migrant_species_flag off

implicit_species_flag on

particle_motion_flag on

particle_forces_option PRIMARY

transverse_weighting_flag on

particle_kinematics_option STANDARD

scattering_flag on

implicit_filtering_parameter 0.1

selection_ratio 0.1

;

species4 ; H2_neut

charge 0
```

```
mass 3672

atomic_number 1

migrant_species_flag off

implicit_species_flag off

particle_motion_flag on

particle_forces_option AVERAGED

transverse_weighting_flag on

particle_kinematics_option STANDARD

scattering_flag on

selection_ratio 1

;

;

[Particle Creation]

;

emission child-langmuir field-stress ; electrons from cathode

 from 5.9  1.1

  to    6.2 2.8 ;1.8

interval 1

species 3

movie_tag 3

discrete_numbers 1 1 1

random on

medium 2

inclusion SOLID

threshold 200.0

breakdown_function 0

charge_factor 1.0

surface_factor 0.66667

thermal_energy 3.0

minimum_charge 0.0

movie_fraction 0.1
```

Appendix: LSP Input Deck

```
;
desorption ; cathode plasma
 from 5.9  1.1
  to   6.2 2.8
;time_interval 0.3 ; was 1600 steps
interval 100
species 4
movie_tag 4
ion_species 0
stimulated_ion_fraction 0.0
thermal_ion_fraction 0.0
electron_species 0
medium 2
monolayers 50
current_flux 2.4e3
threshold FIELD-STRESS 200
binding_energy 70.0
maximum_desorption_rate 1.0
stimulated_cross_section 0.0
sampling_rate 1.0
latency 0.0125 ;0.025
total_number 1
distribution_type SPHERICAL
thermal_energy 3.0
minimum_charge 1.0e-7
movie_fraction 0.0
;
fragmentation ; new ELECTRODE_PLASMA model
 from 5.8 1.0
  to   6.3 2.9
interval 1
```

```
species 4

first_product_species 3

second_product_species 2

movie_tag 3

eos_density 1.0e17

thermal_energy 3.0

movie_fraction 1

;

secondary ; electron creation in foil from ITS

 from 0.0,  -0.05

 to   9.0,   0.05

 interval 1

 species 3

 medium 1

 movie_tag 0

 movie_fraction 0.0

;

emission child-langmuir thermal ; anode parts

 from 0.0  -0.1

 to   9.0  0.1

interval 40

species 2

discrete_numbers 1 1 1

random on

medium 1

inclusion SOLID

threshold 5.0 ; should be 400 or 700

breakdown_function 0

charge_factor 1.0

surface_factor 1.0

thermal_energy 1.0
```

```
minimum_charge 0.0
;
plasma
 from 5   0.03
 to    7.5   0.43
species 1
movie_tag 1
unbound off
discrete_numbers 4 1 4
random off
multiple_numbers 1
cloud_radius 0
density_function 4
momentum_function 0
reference_point 0 0 0
density_flags 0 0 0
momentum_flags 0 0 0
drift_momentum 0 0 0
rotation off
thermal_energy 0
random_energy_function 0
spatial_function 0
movie_fraction 0.1
;
[Particle Interaction]
interaction_files
 interH2H2+.tab
end
;
[MediumModels]
medium1 ; foil
```

```
method 1
type DENSE
dielectric_constant 1.0
surface_conductivity 0.0
permeability 1.0
species 3 ; PRIMARY_SPECIES
density 1.2 ; g/cc
thickness 0.01
temperature 0.0
collision_energies 100
minimum_energy 5.0E+003
maximum_energy 5.0E+006
scattering on
scatter_angles 25
poloidal_angles 25
energy_loss on
dedx_scattering off
components
carbon fraction 1.0
end
energy_units EV
;
medium2 ; Cathodes
method 0
type DENSE
dielectric_constant 1.0
surface_conductivity 0.0
permeability 1.0
temperature 300.0
conductivity off
energy_units EV
```

Appendix: LSP Input Deck

```
;
;
[Boundaries]
;
outlet ; drive function
from   10.0, 1.226
to     10.0, 3.0
phase_velocity 1
drive_model POTENTIAL
potentials
   1   0.0
   2   1.0
end
circuit 0
temporal_function 2 ; voltage drive
time_delay 0.0
;
;
[Functions]
function2 ; idealized voltage drive.
type 0 data_pairs
 0.0 0.0
 5.0 3.0778e3
end
;
function4; neutral density
type 0
data_pairs
 0 5e16
 100 5e16
end
```

Appendix: LSP Input Deck

```
;
;
[Probes]
;
probe1 energy field_flux
probe2 energy particle_flux
probe3 energy field_energy
probe4 energy particle_energy
probe5 energy total_energy
probe6 energy net_energy
;
probe7
label "Vin r=8cm"
voltage
from 9.9 0 1.6
to   9.9 0 3.1
;
probe8
label "Iin r=8cm"
current
from 9.9 0.0 2.9
to   9.9 0.0 2.9
;

probe9  global number species 1
probe10 global number species 2
probe11 global number species 3
;
probe12 global charge species 1
probe13 global charge species 2
probe14 global charge species 3
```

```
;
probe15 global ketot species 1
probe16 global ketot species 2
probe17 global ketot species 3
;
probe18 global ocmax species 1
probe19 global opmax species 1
;
probe20
particle species 2
dqdt
direction Z
at 0.0 1.0
;
probe21
particle species 2
dqdt
direction Z
at 0.0 4.0
;
probe22
particle species 2
kenergy
direction Z
at 0.0 1.0
;
probe23
particle species 2
kenergy
direction Z
at 0.0 4.0
```

```
;
probe24   global number species 1
probe25 global charge species 1
probe26 global ketot species 1
probe27 global opmax species 1
;
```

References

[1] H. A. Davis, R. R. Bartsck, J. C. Olson, D. J. Rej, and W. J. Waganaar. Intense ion beam optimization and characterization with infrared imaging. *Journal of Applied Physics*, 82(7):3223–3231, October 1997.

[2] P. Mistry, C. Hill, J. O'Malley, J. Precious, M. Ellis, R. Maddock, F. C. Young, S. L. Jackson, D. G. Phipps, R. Woolf, and B. Phlips. Photofission for active snm detection ii: Intense pulsed ^{19}f(p,$\alpha\gamma$)^{16}o characteristic γ source. In *Nuclear Science Symposium and Medical Imaging Conference (NSS/MIC), 2012 IEEE*, pages 24–31, Anaheim, CA, USA, Oct. 27–Nov. 03 2012. Institute of Electrical and Electronic Engineers.

[3] R. A. Meger and F. C. Young. Pinched-beam ion-diode scaling on the aurora pulser. *Journal of Applied Physics*, 53(12):8543–8548, December 1982.

[4] P. A. Miller and C. W. Mendel Jr. Analytic model of applied-b ion diode impedance behavior. *Journal of Applied Physics*, 61(2):529–539, January 1987.

[5] S. Humphries Jr. Intense pulsed ion beams for fusion applications. *Nuclear Fusion*, 20(12):1549–1612, December 1980.

[6] G. Cooperstein, Shyke A. Goldstein, R. A. Meger, D. Mosher, W. F. Oliphant, F. L. Sandel, S. J. Stephanakis, F. C. Young, and H. U. Karow. Light ion production and focusing with pinch-reflex diodes. In *PROCEEDINGS OF THE 4th INTERNATIONAL TOPICAL CONFERENCE ON HIGH-POWER ELECTRON AND ION-BEAM RESEARCH AND TECHNOLOGY*, pages 53–60, Palaiseau, France, Jun. 29–Jul. 03 1981. Institute of Electrical and Electronic Engineers.

[7] D. D. Hinshelwood, P. F. Ottinger, J. W. Schumer, R. J. Allen, J. P. Apruzese, R. J. Commisso, G. Cooperstein, S. L. Jackson, D. P. Murphy, D. Phipps, S. B. Swanekamp, B. V. Weber, and F. C. Young. Ion diode performance on a positive polarity inductive voltage adder with layered magnetically insulated transmission line flow. *Physics of Plasmas*, 18(5):053106, May 2011.

[8] G. Cooperstein, Shyke A. Goldstein, R. A. Meger, D. Mosher, W. F. Oliphant, F. L. Sandel, S. J. Stephanakis, F. C. Young, and H. U. Karow. Generation

References

and focusing of intense light ion beams from pinched-electron beam diodes. In *PROCEEDINGS OF THE 3rd International Topical Conference on HIGH POWER ELECTRON AND ION BEAM Research and Technology VOLUME II*, pages 567–575, Novosibirsk, USSR, Jul. 03–Jul. 06 1979. Institute of Electrical and Electronic Engineers.

[9] Tetsu Ozaki, Shyuji Miyamoto, Kazuo Imasaki, Sadao Nakai, , and Chiyoe Yamanaka. Generation and focusing of intense ion beams in pinch-reflex diode. *Japanese Journal of Applied Physics*, 20(11):L843–L846, November 1981.

[10] J. N. Olsen and R. J. Leeper. Ion beam tranport in laser-initiated discharge channels. *Journal of Applied Physics*, 53(5):2879–2887, May 1982.

[11] Shyke A. Goldstein, G. Cooperstein, Roswell Lee, D. Mosher, and S. J. Stephanakis. Focusing of intense ion beams from pinched-beam diodes. *Physical Review Letters*, 40(23):1504–1507, June 1978.

[12] J. W. Maenchen, F. C. Young, R. Stringfield, S. J. Stephanakis, D. Mosher, Shyke A. Goldstein, R. D. Genuario, and G. Cooperstein. Production of intense light ion beams on a multiterawatt generator. *Journal of Applied Physics*, 54(1):89–100, October 1983.

[13] E. Nardi, E. Peleg, and Z. Zinamon. Energy deposition by fast protons in pellet fusion targets. *Physics of Fluids*, 21(4):574–579, April 1978.

[14] D. S. Prono, H. Ishizuka, E. P. Lee, B. W. Stallard, and W. C. Turner. Charge-exchange neutral-atom filling of ion diodes: Its effect on diode performance and a-k shortening. *Journal of Applied Physics*, 52(4):3004–3011, April 1981.

[15] D. G. Colombant and Shyke A. Goldstein. Anode-plasma expansion in pinch-reflex diodes. *Physical Review Letters*, 51(17):1562–1565, October 1983.

[16] A. E. Blaugrund, G. Cooperstein, and A. Goldstein Shyke. Relativistic electron beam pinch formation processes in low impedance diodes. *Physics of Fluids*, 20(7):1185–1194, July 1977.

[17] T. D. Pointon. Charge exchange effects in ion diodes. *Journal of Applied Physics*, 66(7):3397–3404, October 1989.

[18] D. R. Welch, D. V. Rose, M. E. Cuneo, R. B. Campbell, and T. A. Melhorn. Integrated simulation of the generation and transport of proton beams from laser-target interaction. *Physics of Plasmas*, 13(6):063105, June 2006.

[19] R. Courant, K. Friedrichs, and H. Lewy. On the partial difference equations of mathematical physics. AEC Research and Development Report NYO-7689, AEC COmputing Facility Institute of Mathematical Sciences, P.O. Box 5800, Albuquerque, NM., 87185, September 1956.

References

[20] M. S. DiCapua and D. G. Pellinen. Propagation of power pulses in magnetically insulated vacuum transmission lines. *Journal of Applied Physics*, 50(5):3713–3720, May 1979.

[21] M. E. Cuneo. The effect of electrode contamination, cleaning and conditioning on high-energy pulsed-power device performance. *Proceedings of the IEEETDEI*, 66(4):469–485, August 1999.

[22] K. W. Bieg, E. J. T. Burns, J. N. Olsen, and L. R. Dorrell. Ion source studies for particle beam accelerators. *Journal of Vacuum Science Technology A*, 3(3):1234–1237, June 1985.

[23] V. K. Tripathi, P. F. Ottinger, and J. Guillory. Thermal-resistive current filamentation in the cathode plasma of a pinch-reflex diode. *Journal of Applied Physics*, 54(6):3043–3048, June 1983.